Batteries & Supercaps

Research Article
doi.org/10.1002/batt.202200035

Chemistry Europe
European Chemical Societies Publishing

www.batteries-supercaps.org

Special Collection

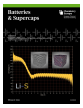

Investigation of the Effect of Temperature on Lithium-Sulfur Cell Cycle Life Performance Using System Identification and X-Ray Tomography

Neda Shateri,[a] Daniel J. Auger,[a] Abbas Fotouhi,*[a, c] James Brighton,[a] Wenjia Du,[b, c] Rhodri E. Owen,[b, c] Dan J. L. Brett,[b, c] and Paul R. Shearing[b, c]

In this study, cycle life performance of a prototype lithium-sulfur (Li–S) pouch cell is investigated using system identification and X-ray tomography methods. Li–S cells are subjected to characterization and ageing tests while kept inside a controlled-temperature chamber. After completing the experimental tests, two analytical approaches are used: i) The parameter variations of an equivalent-circuit model due to ageing are determined using a system identification technique. ii) Physical changes of the aged Li–S cells are analyzed using X-ray tomography. The results demonstrate that Li–S cell's degradation is significantly affected by temperature. Comparing to 10 °C, Li–S cell capacity fade happens 1.4 times faster at 20 °C whereas this number increases to 3.3 at 30 °C. In addition, X-ray results show a significant swelling when temperature rises from 10 to 20 °C, correspondingly the gas volume increases from 13 to 62 mm^3.

Introduction

Battery technology development has a remarkable impact on the existing vehicle electrification trends. Among various battery technologies which are under development, one promising technology is lithium-sulfur (Li–S) with advantages like improved safety, low cost, and more importantly, higher energy density,[1,2] However, Li–S technology still needs further improvement before being ready for large-scale commercialization, mainly due to its low cycle life.[3] That is particularly important for applications like electric road vehicles by considering their requirements,[4] unmanned aerial vehicles (UAVs) and electric passenger aircrafts as discussed by Dörfler et al.[6] On the other hand, there have been lots of achievements in improvement of Li–S cells during the recent years.[5,6] An example of such achievements is presented by Huang et al.,[7] and the development of a Li–S cell with up to 1000 cycles is reported. In addition to the studies which are focused on improvement of Li–S cell's performance, Battery Management System (BMS) developers are trying to build necessary algorithms for real applications of that technology.[8–15] Within that scope, the present study aims at investigation of the effect of temperature on Li–S cell's performance and its cycle life.

Li–S cell degradation mechanism is a subject of study in the electrochemical literature. In the work by Canasa et al.,[16] Electrochemical impedance spectroscopy (EIS) technique is applied to analyze the degradation mechanism of Li–S cell by monitoring the parameters of an equivalent circuit network (ECN) model, and their relationship with the physical and chemical processes which are taking place in the cathode, anode and electrolyte. Various materials are investigated with respect to their impacts on Li–S cell's life, aiming at cycle life improvement.[17] In couple of other studies,[18,19] the effect of various cathode binders on Li–S cell's performance is investigated. Moreover, Li–S cell's degradation mechanism is studied by focusing on surface morphologies and the cathode's chemical structure.[4] In addition, Scanning Electron Microscopy, X-ray Photoelectron Spectroscopy, and Near Edge X-ray Absorption Fine Structure techniques are discussed in[20–22] for the same goal. Recently, X-ray tomography has been applied to complement other techniques,[19] providing dynamic information across multiple scales including morphological evolution[23,24] and phase distributions.[25] These studies mainly focused on the carbon-sulfur electrode to the particle level and a bespoke environment is needed for in-situ 3D characterization. However, X-ray imaging of Li–S pouch cells with realistic electrolyte loadings at the macroscale is yet to be widely realized with very limited reports in open literature.

Although Li–S cell ageing due to cycling is widely investigated in the literature from an electrochemical point of view, there are not many studies in which that phenomenon is studied from the perspective of battery management in applications.[26] Although the electrochemical models can help

[a] N. Shateri, Dr. D. J. Auger, Dr. A. Fotouhi, Prof. J. Brighton
Advanced Vehicle Engineering Centre
Cranfield University
Bedfordshire, MK43 0AL, UK
E-mail: a.fotouhi@cranfield.ac.uk
[b] Dr. W. Du, Dr. R. E. Owen, Prof. D. J. L. Brett, Prof. P. R. Shearing
The Electrochemical Innovation Lab, Department of Chemical Engineering
University College London
London, WC1E 7JE, UK
[c] Dr. A. Fotouhi, Dr. W. Du, Dr. R. E. Owen, Prof. D. J. L. Brett, Prof. P. R. Shearing
The Faraday Institution, Quad One
Harwell Campus, Didcot OX11 0RA, UK

Special Collection An invited contribution to a Special Collection dedicated to Lithium–Sulfur Batteries

© 2022 The Authors. Batteries & Supercaps published by Wiley-VCH GmbH. This is an open access article under the terms of the Creative Commons Attribution License, which permits use, distribution and reproduction in any medium, provided the original work is properly cited.

© 2022 The Authors. Batteries & Supercaps published by Wiley-VCH GmbH

a lot to better understand the ageing mechanisms of different batteries, such high-fidelity models are not necessarily helpful for real-time applications due to their additional computational cost. Example studies of the Li–S BMS are presented in previous reports,[27,28] where an experimental methodology is used to investigate Li–S cell ageing. One of the restrictions in those previous studies is related to the cycling charge/discharge current profiles, which are not based on a realistic duty cycle. In the present study however, the cells are subjected to a more realistic degradation scenario, which is an EV driving cycle test. Furthermore, the Li–S cells which had been used previously[27,28] were of a lower capacity type (i.e., 3.4 Ah) whereas in this study, a new high capacity (i.e., 19 Ah) Li–S cell is investigated. For example, the impact of ageing on cell's capacity and internal resistance are studied.[28] Although the outcome of that study is promising, it suffers from having access to real-world test data. That restriction is eliminated in the present study by performing EV driving cycle test scenarios.

Although the literature of Li–S BMS is not very rich, there are many studies on aging modeling of Lithium-ion cells. A couple of examples are reported[29,31] where a cycle life model is established for a graphite-$LiFePO_4$ cell by considering the effects of depth of discharge, temperature and discharge rate. According to the literature, temperature has a significant impact on the cycle life of lithium-ion batteries. The best cycle life performance is obtained for mild temperatures however, it is shown in different works that it can vary based on the type of the cell too. For example, the optimal cycling temperature of lithium-ion cells is found out to be around 25 °C[30] where experimental tests were conducted at temperature range between −20 °C and 70 °C on 18650-type cells with a $Li_xNi_{1/3}Mn_{1/3}Co_{1/3}O_2/Li_yMn_2O_4$ blended cathode and graphite/carbon anode. Other similar studies have reported an optimal cycling temperature for lithium-ion batteries as well, though the numbers slightly vary among them.[31,32] According to the literature, a temperature higher than the optimal value can cause an accelerated solid electrolyte interphase formation and thus, a more rapid capacity fade and impedance rise would happen,[33–35] On the other hand, lower temperatures favor lithium plating at the end of the charging process. Consequently, the cycle life decreases due to intensified lithium plating. Many researchers have identified lithium plating using either in-situ or ex-situ methods in cycled lithium-ion cells at low temperatures.[36–42]

As mentioned above, the literature suffers from lack of studies on the effect of temperature on Li–S battery cycle life performance, motivating this present study. This paper investigates the influence of temperature, as a stress factor, on Li–S pouch cells' cycling performance using an experimental approach, which has not been reported in the literature at the best knowledge of the authors.

Looking at the literature, the contributions of this study are as follows.

i) Real-world charge/discharge experimental data of a new high-capacity Li–S pouch cell at different temperatures is presented and analyzed.
ii) The effects of cycling on Li–S cell's performance (i.e., capacity fade and power fade) are investigated using an ECN model and a system identification technique by considering the effect of temperature.
iii) Physical changes of Li–S cell due to cycling is analyzed with a focus on the effect of temperature. X-ray tomography analysis is performed on fresh and aged Li–S pouch cells for the first time.

Experimental and Modelling Section

Li-S cell specifications

The Li–S cells that are tested in this study, were manufactured and supplied by OXIS Energy Ltd.[43] Specifications of the 19 Ah prototype Li–S cell are listed in Table 1.

Li-S cell testing

The test rig includes a bidirectional power source to apply any desired charge/discharge current profile, and a thermal chamber (shown in Figure 1a) to control the temperature. In terms of measurements, the cell's terminal voltage and current signals are recorded at a sampling rate of 1 Hz. All tests are performed within the full range of SoC based on a cut-off voltage of 1.9 V and fully-charged voltage of 2.6 V.

A charge/discharge profile is obtained according to the required power on the Millbrook London Transport Bus (MLTB) driving cycle,[44,45] which is scaled down to a single cell level as discussed in previous literature.[46] An example MLTB test result at 20 °C is shown in Figure 1(b) where the test cycle is repeated until zero SoC. Figure 1(b) shows a zoomed window of a single MLTB cycle as well. The negative current values in that figure represent regenerative braking.

Li-S cell modelling

The Thevenin equivalent-circuit-network (ECN) model structure[50] is used in this study because of its proper trade-off between accuracy and computational speed[47–49] as shown in Figure 1(c). The model contains a voltage source U_{OC}, and physical components such as ohmic resistance (R_O), polarization resistance (R_P) and polarization capacitance (C_P). Mathematical presentation of this model is as follows:

$$U_L = U_{oc} - U_p - R_0 I_L \tag{1}$$

$$\frac{dU_p}{dt} = -\frac{1}{R_p C_p} U_p + \frac{1}{C_p} I_L \tag{2}$$

Table 1. Li–S cell specifications.

Parameter	Value
Capacity	19 (Ah)
Nominal voltage	2.15 (V)
Cell mass	141 (g)
Maximum voltage	2.6 (V)
Minimum voltage	1.9 (V)
Maximum discharge rate	3 C∼57 (A)
Maximum charge rate	0.25 C∼4.75 (A)

© 2022 The Authors. Batteries & Supercaps published by Wiley-VCH GmbH

Research Article
doi.org/10.1002/batt.202200035
Chemistry Europe
European Chemical Societies Publishing

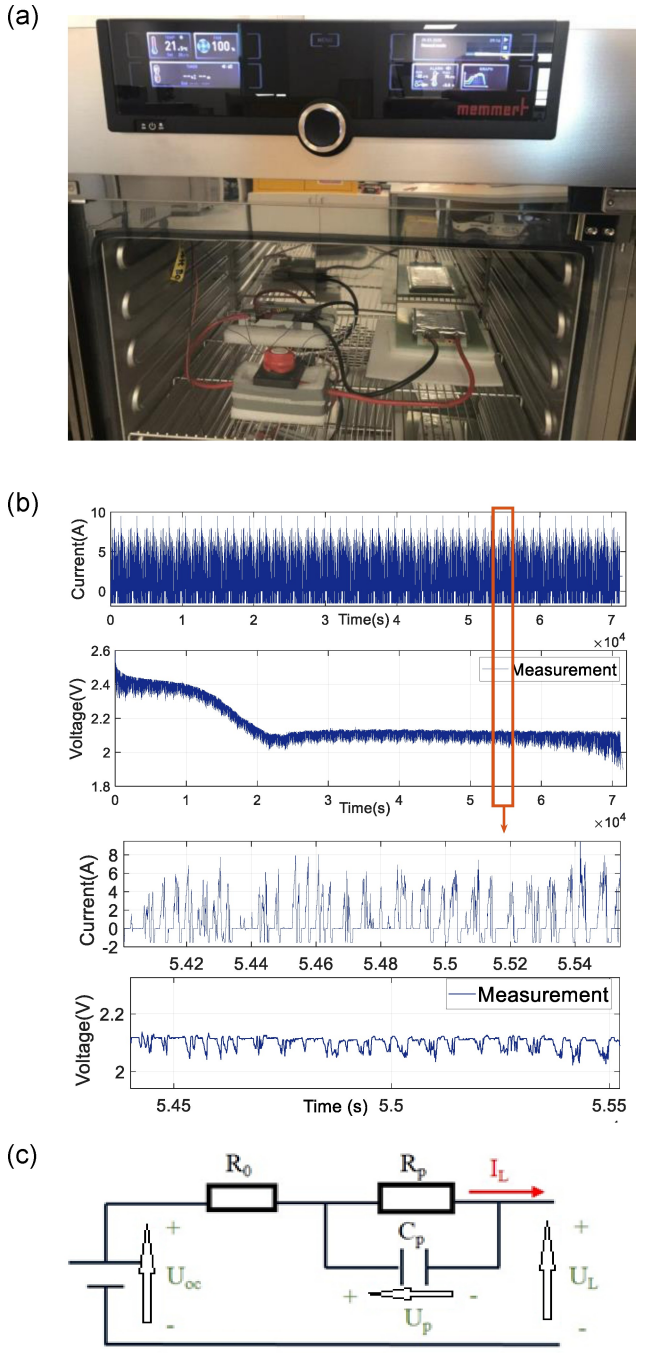

Figure 1. Li–S cell test and modelling: a) Li–S cell inside a thermal chamber, b) Li–S cell's terminal voltage and current signals during an example MLTB test, c) Thevenin model.

where U_L and I_L are the battery terminal voltage and load current, respectively, whereas U_p is the voltage across the polarization capacitor.

Applying the Laplace transform to Equation (2), we have:

$$s \cdot U_p(s) = -\frac{1}{R_p C_p} \cdot U_p(s) + \frac{1}{C_p} I_L(s) \tag{3}$$

Consequently, U_p can be expressed as:

$$U_p(s) = \frac{\frac{1}{C_p} I_L(s)}{s + \frac{1}{R_p C_p}} \tag{4}$$

We can then obtain the terminal voltage by substituting U_p from Equation (4) into Equation (1):

$$U_L(s) = U_{oc} - \frac{\frac{1}{C_p} I_L(s)}{s + \frac{1}{R_p C_p}} - R_0 I_L(s) \tag{5}$$

Applying the bi-linear transform of $s = \frac{2}{T}\frac{z-1}{z+1}$, Equation (5) can be discretized as follows.

$$\frac{U_L(z) - U_{oc}}{I_L(z)} = \frac{-\left(TR_p + TR_0 + 2R_0R_pC_p\right) - \left(TR_p + TR_0 - 2R_0R_pC_p\right)z^{-1}}{T + 2R_pC_p + \left(T - 2R_pC_p\right)z^{-1}} \tag{6}$$

Then the terminal voltage at moment k, is obtained as follows:

$$U_L(k) = \theta_1 \cdot U_L(k-1) + \theta_2 \cdot I_L(k) + \theta_3 \cdot I_L(k-1) + \theta_4 \tag{7}$$

where the parameters $\theta_1, \theta_2, \theta_3$ and θ_4 are:

$$\theta_1 = \frac{2R_pC_p - T}{T + 2R_pC_p} \tag{8}$$

$$\theta_2 = -\frac{TR_p + TR_0 + 2R_0R_pC_p}{T + 2R_pC_p} \tag{9}$$

$$\theta_3 = -\frac{TR_p + TR_0 - 2R_0R_pC_p}{T + 2R_pC_p} \tag{10}$$

$$\theta_4 = \frac{2T}{T + 2R_pC_p} U_{oc} \tag{11}$$

Writing Eq. (7) in a more standard way, we have:

$$U_L(k) = \varphi^T \cdot \theta \tag{12}$$

where $\varphi = [U_L(k-1); I_L(k); I_L(k-1); 1]$ and $\theta = [\theta_1; \theta_2; \theta_3; \theta_4]$.

In this study, the Forgetting Factor Recursive Least Square (FFRLS) identification algorithm[51,52] is used to obtain the Thevenin model's parameters R_0, R_p, C_p and U_{oc}. Looking at the literature, there are several studies in which the EIS technique is used to parameterize a battery model. Specifically for Li–S battery, both EIS[53–57] and System Identification[12–15] methods have been already used in the literature. For example,[53,54] an electrical circuit model is considered to simulate the electrochemical behavior of Li–S batteries and to measure their impedance over 50 cycles. In previous reports,[55,56] EIS technique is utilized for capacity fade analysis of sulfur cathodes in Li–S cells. Furthermore, a 3.4 Ah pouch Li–S cell is investigated[57] using the EIS technique, and the effects of SoC and temperature on model parameters are demonstrated.

In this study however, the FFRLS system identification method is used instead of EIS. Comparing the two techniques, EIS might be more accurate in terms of providing the electrochemical details of the cell however, our system identification technique is quicker in

© 2022 The Authors. Batteries & Supercaps published by Wiley-VCH GmbH

Research Article
doi.org/10.1002/batt.202200035
Chemistry Europe
European Chemical Societies Publishing

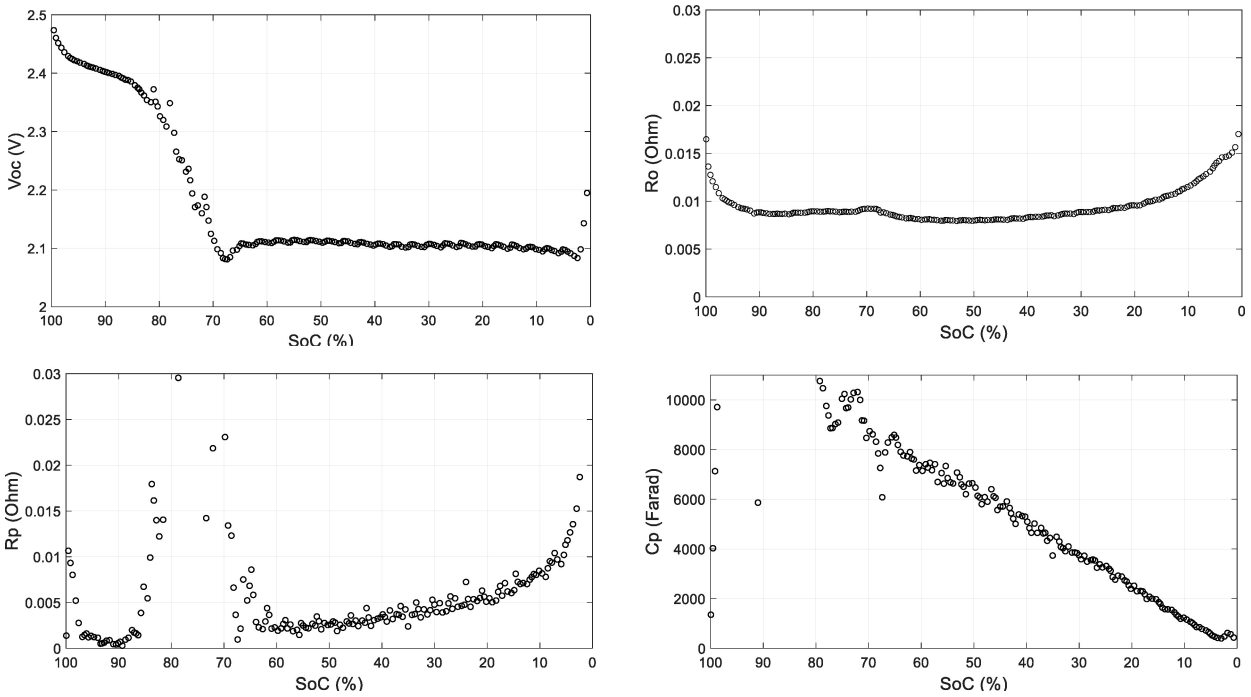

Figure 2. Li–S cell Thevenin model's parameters vs. SoC at 20 °C for a fresh cell.

real-time applications. For that reason, we decided to use FFRLS technique to be easily implemented in BMS boards.

The parameters vector θ is updated at each iteration as follows:

$$\widehat{\theta}(k) = \widehat{\theta}(k-1) + K(k) \cdot [U_L(k) - \varphi^T \cdot \widehat{\theta}(k-1)] \tag{13}$$

where K is called 'correction gain' and is calculated as follows:

$$K(k) = P(k-1) \cdot \varphi \cdot [\gamma + \varphi^T \cdot P(k-1) \cdot \varphi]^{-1} \tag{14}$$

$$P(k) = \frac{1}{\gamma}[I - K(k) \cdot \varphi^T] \cdot P(k-1) \tag{15}$$

where P is the covariance matrix and γ is the forgetting factor, which indicates the effect of historical data on the identification results.

Figure 2 shows an example identification result for a fresh Li–S cell at 20 °C. As shown in the figure, each parameter of the Thevenin model has a unique pattern vs. SoC. The patterns which are obtained in this study, agree with what has been already published in the literature.[9–13]

Figure 3 demonstrates an example test for validation of the identified model. In that figure, cell's simulated terminal voltage is plotted against the measured value. According to the results, there is a good fit between the model and the experimental data.

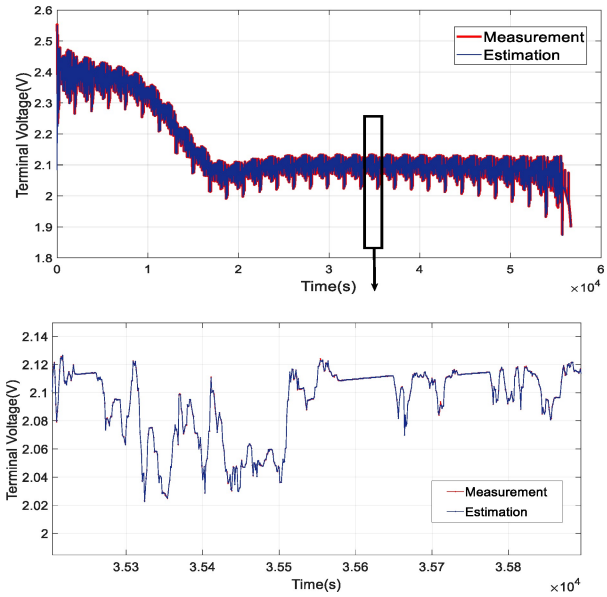

Figure 3. Li–S cell model's terminal voltage vs. experimental data.

X-ray computed tomography

A lab-based X-ray CT scanner (Nikon XT 225, Nikon Metrology, UK) was used to investigate the 19 Ah Li–S pouch cells (dimension: 148×80×12.5 mm^3). The experimental setup is shown in Figure 4. A plastic holder was fabricated by a 3D printer (Ultimaker S3) to accommodate the pouch cell sample and to prevent subtle movement during X-ray acquisition. A polychromatic cone-beam source employing a tungsten target with the voltage and power set at 100 kV and 20 W were used with an exposure time of 1 second per projection, and a total of 3185 projections were collected per tomogram with a 1 mm Cu filter. The 2028×2028-pixel CCD camera detector was binned 1 to achieve the voxel resolution at ca. 20 µm with a field of view of ca. 40×40 mm^2. The raw X-ray projections were reconstructed using Nikon CT Pro 3D software (Version XT 4.4.4, Nikon Metrology, Tring, UK). Three Li–S samples were scanned using the same X-ray parameters, namely fresh, aged at 10 °C, aged at 20 °C. The details of the interior X-ray tomography are summarized in Table 2.

© 2022 The Authors. Batteries & Supercaps published by Wiley-VCH GmbH

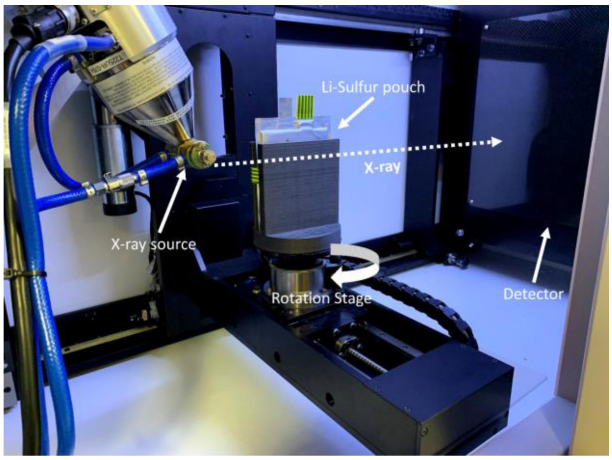

Figure 4. The experimental setup of X-ray imaging for a 19 Ah lithium-sulfur pouch cell by using the Nikon XTH 225 scanner at EIL and the bespoke 3D printed sample holder was used to accommodate sample.

X-ray images processing

The reconstructed tomograms were initially cropped to remove the unwanted border and highlight the region of interest (ROI) before importing into Dragonfly (ORS, Montreal, Canada) for subsequent image processing. The Gabor filter was used to further improve the image quality before image segmentation and visualization. Afterwards, quantifications were performed and obtained, including surface area, volume, and thickness of gas layers, etc. Thickness was measured by agglomerating connected voxels and measuring the dimensions of each aggregate. After image binarization, the gas phase is segmented using Otsu method, and then the thickness module in software is used to calculate the thickness according to the labelled pixels. More details of the thickness measurement approach can be found.[69] It should be noted that 1) the thickness distributions of gas in 3D were correspondingly superimposed on their raw rendered datasets; 2) it is difficult to accurately determine the gas thickness in the fresh cell because of the limitation of resolution by macro-CT.

Results and Discussion

Capacity fade and power fade of Li-S Cell due to ageing at various temperatures

In this Section, the effect of temperature on Li–S cell degradation is analyzed with a focus on cell's capacity fade and power fade. For performing such an analysis, first the battery end-of-life (EoL) is formulated based on two definitions.[61] In the first definition, the remaining life of a battery is calculated based on capacity fade as a fraction of its original capacity (Q_{init}). In that definition, EoL is when the battery capacity (Q_{batt}) drops to 80% of the initial capacity. Therefore, battery state-of-health (SoH) is formulated as follows:

$$\begin{aligned} &SoH_Q = 1 - \ (Q_{init} - Q_{batt})/(0.2\ Q_{init}), \\ &0.8\ Q_{init} \le Q_{batt} \le Q_{init} \end{aligned} \tag{16}$$

where SoH_Q varies between 1 and 0 corresponding to a fresh battery and EoL respectively (i.e., $Q_{batt} = 0.8\ Q_{init}$ at EoL). So, this definition is based on the battery's "capacity fade" as an indicator of the degradation process.

Another possible definition of SoH corresponds to "power fade". This is somehow related to another term in the literature called battery State-of-Power (SoP).[62,63] The deliverable battery power very much depends on its ohmic resistance, which is a function of its age. In general, ageing mechanism causes an increase in the ohmic resistance, which can be used as an indicator of battery SoH.[64] If we define battery EoL at the point where its resistance doubles, battery SoH is formulated as follows:[61]

$$SoH_R = 1 - \ (R_{batt} - \ R_{init})/R_{init}, \ R_{init} \le R_{batt} \le 2R_{init} \tag{17}$$

where R_{init} is the battery's initial resistance and R_{batt} is the resistance value at a given time. Similar to SoH_Q, SoH_R also varies between 1 and 0.

Figure 5(a) depicts capacity fade of the Li–S cell subject to cycling at different temperatures. In those experiments, the Li–S cells were subjected to the MLTB discharge profile repeatedly until the cell is degraded. At each cycle, a limited number of MLTB repetitions are applied to the cell consecutively from full-charged state until depleted state, and then the cell is charged again at rate of 0.1 C (i.e., 1.9 A) to make it ready for the next cycle. The whole test procedure was repeated for identical cells at three different temperatures. We should clarify that although the cells are identical in terms of specifications, because they are prototypes, there are small differences between cells initial capacities. That issue is expected to disappear when moving to automated mass production procedures.

According to the result shown in Figure 5(a), temperature has a significant impact on the rate of capacity fade in a Li–S cell when subjected to cycling. As shown in the figure, the best performance is achieved at 10 °C with the lowest rate of capacity fade. On the other side, the fastest degradation rate is observed at 30 °C. Comparing 10 and 20 °C temperatures, it is observed that Li–S cell capacity fade happens 1.4 times faster at 20 °C whereas this number increases to 3.3 times faster at 30 °C. Figure 5(b) shows the same results in a different format, that is SoH_Q, calculated using Equation (16).

Table 2. The X-ray CT acquisition parameters for the 19 Ah Li–S pouch cells.

Scan No	Cyclic status	Resolution [μm]	Voltage [kV]	Power [W]	Exposure time [s]	Projection No.	FOV [mm^2]
1	Fresh	20	100	20	1	3185	40×40
2	Aged at 10 °C	20	100	20	1	3185	40×40
3	Aged at 20 °C	20	100	20	1	3185	40×40

© 2022 The Authors. Batteries & Supercaps published by Wiley-VCH GmbH

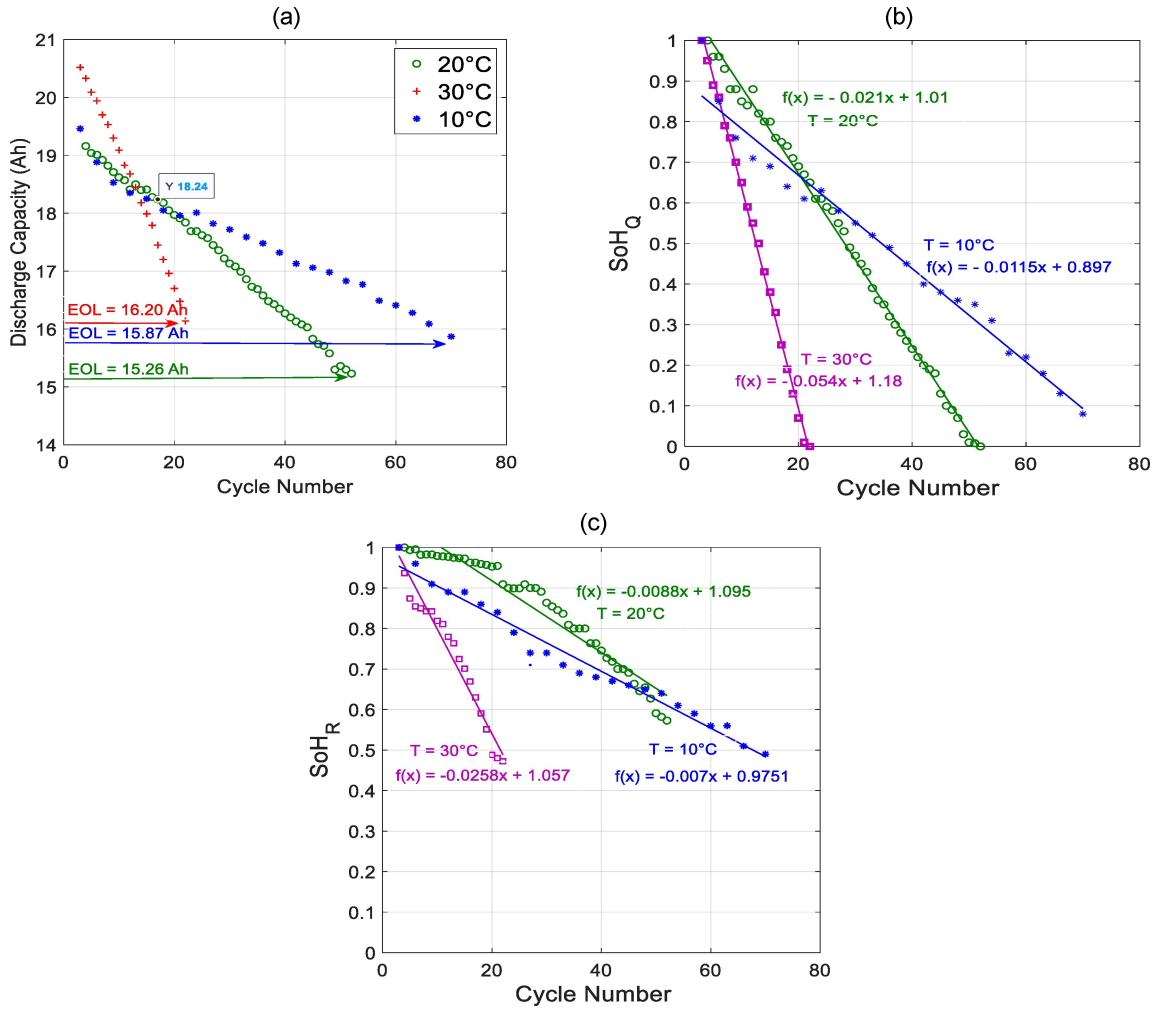

Figure 5. a) definition of EoL according to 20% capacity fade, b) **SoH_Q**: Li–S cell SoH based on capacity fade, c) **SoH_R**: Li–S cell SoH based on power fade.

In addition, Figure 5(c) depicts another interesting outcome of the ageing tests. In that figure, the values of SoH_R are calculated using Equation (17). According to the results, the minimum value of SoH_R does not reach to zero. The reason is that Li–S cell power fade happens at a much slower rate than capacity fade. That is one of the most interesting results of this study, specifically for the real applications in which a consistent power delivery is important. In terms of the comparison between temperatures, still the best performance is achieved at 10 °C whereas the worst case happens at 30 °C.

Performance change of Li-S cell due to ageing at various temperatures

In order to investigate the effect of temperature on Li–S cell's performance, ageing tests as well as model identification procedure are repeated at different temperatures. Figure 6 shows the identification results at 10 °C and different age levels in form of the Thevenin model's parameters vs. SoC. According to the results, parameters R_0 and C_p are more sensitive to the cycling while the other two parameters, U_{oc} and R_p, are more stable. The ohmic resistance, R_0, is clearly increasing due to ageing, and the polarization capacitance, C_p, slightly decreases as the result of cycling at 10 °C. Further discussions about the reasons behind those changes are presented in "Physical changes of Li–S cell due to ageing at various temperatures" Section based on cell macrostructure examination.

Figures 7 and 8 demonstrate similar analysis at 20 °C and 30 °C respectively. Again, the results show that parameters U_{oc} and R_p have been affected less than the other two parameters R_0 and C_p because of the cycling. The changes in parameters R_0 and C_p become more significant at higher temperatures, which means more capacity and power fades. That is why we can conclude 10 °C as the best and 30 °C as the worst case in terms of Li–S cell's performance degradation due to cycling. To the best of our knowledge, this outcome has not been reported earlier in the literature for a Li–S pouch cell. In addition, Figure 9 illustrates Li–S cell's time constant (i.e., $R_p \times C_p$) at different age levels and temperatures.

According to the results, parameters U_{oc} and R_p have been affected less than parameters R_0 and C_p as the result of cycling. Table 3 quantifies the changes in average value of parameters R_0 and C_p before and after cycling. For example, at 10 °C, the

© 2022 The Authors. Batteries & Supercaps published by Wiley-VCH GmbH

Research Article
doi.org/10.1002/batt.202200035
Chemistry Europe
European Chemical Societies Publishing

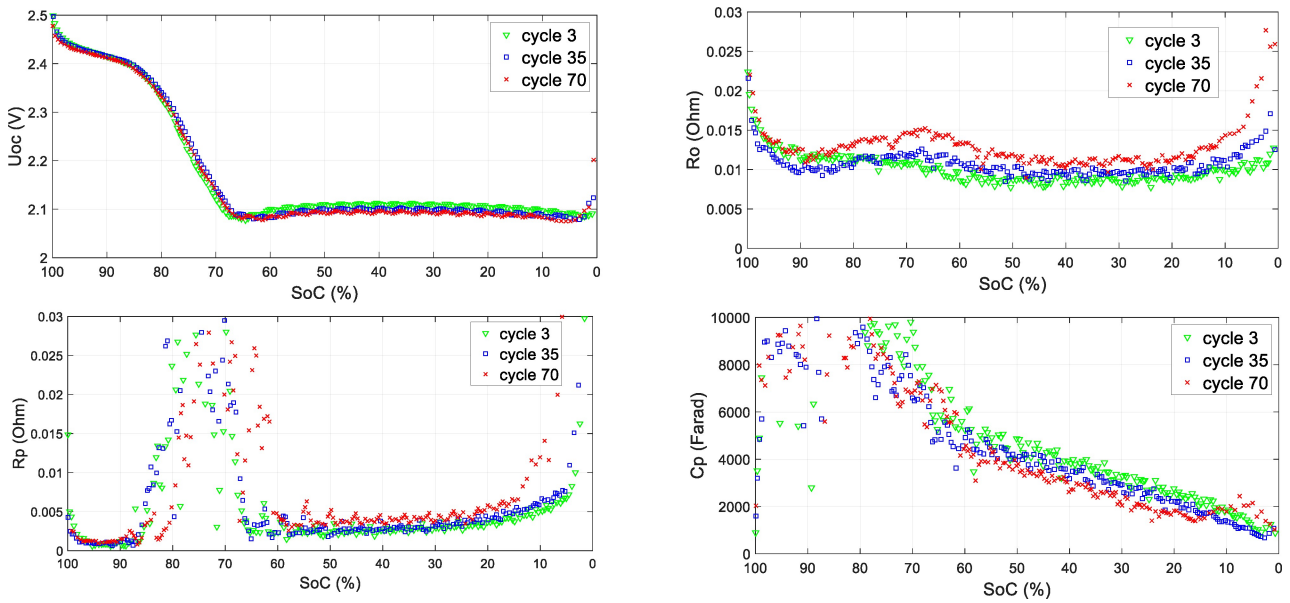

Figure 6. Parameters of Li–S cell model vs. SoC at 10 °C at different age levels.

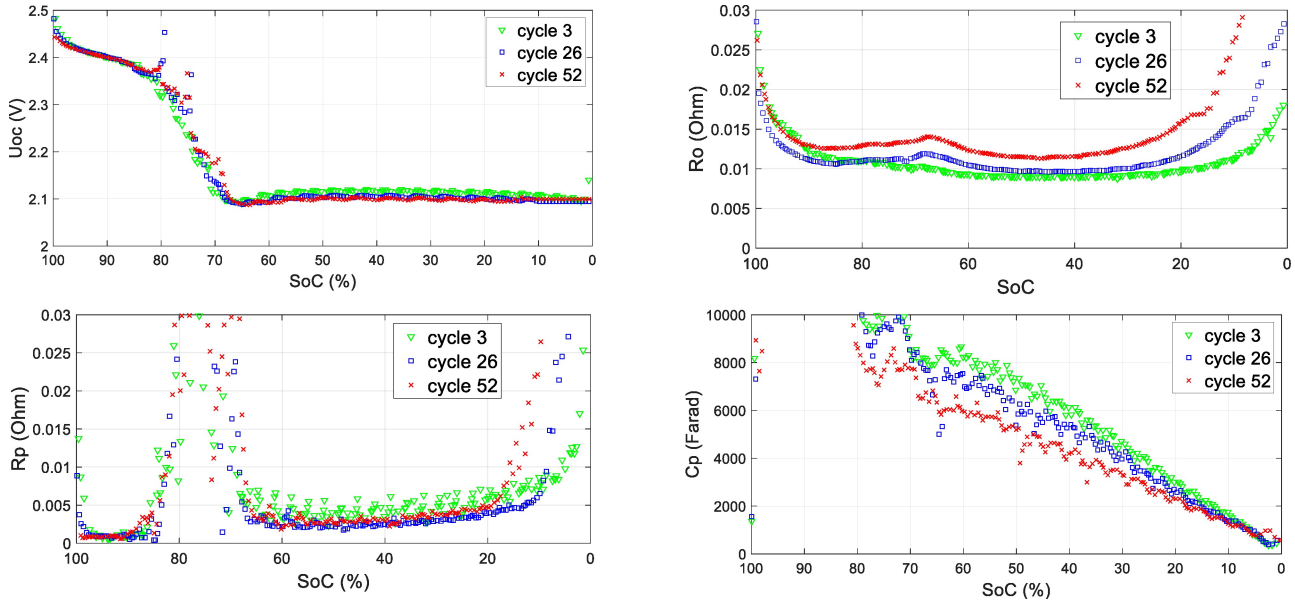

Figure 7. Parameters of Li–S cell model vs. SoC at 20 °C at different age levels.

Table 3. Change in Li–S cell model parameters due to ageing at different temperatures.

Parameter	R_0	C_p
10 °C	40%	−12%
20 °C	42%	−23%
30 °C	53%	−29%

average ohmic resistance has increased 40% due to ageing whereas a decrease of 12% is observed in parameter C_p. The biggest changes are happening at 30 °C where we observe 53% increase in R_0 and 29% decrease in C_p when an aged cell is compared against a fresh cell. As a summary, Figure 10 shows how the parameters R_0 and C_p change due to cycling at three temperatures and two SoC levels.

Although the whole results of this study are not directly comparable to what had already been published in the literature, it is useful to mention the most relevant studies here again. In terms of capacity fading and number of cycles, which were presented in the previous "Capacity fade and power fade of Li–S cell due to ageing at various temperatures" Section, the results are compared as follows. For example[53,54] 50 cycles are reported for a Li–S coin cell where the specific discharge capacity has dropped from 1200 mAh/g to 240 mAh/g (i.e., 80% capacity loss). In another study,[55] capacity fade is reported between 30% and 60% after 100 cycles for Li–S coin

© 2022 The Authors. Batteries & Supercaps published by Wiley-VCH GmbH

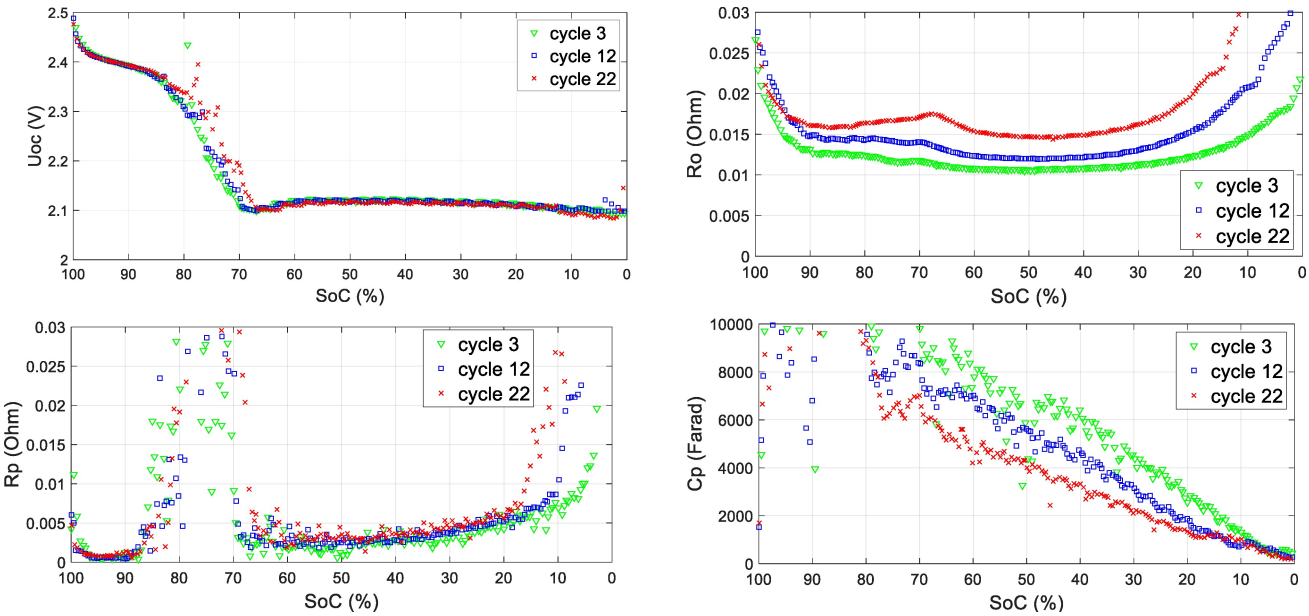

Figure 8. Parameters of Li–S cell model vs. SoC at 30 °C at different age levels.

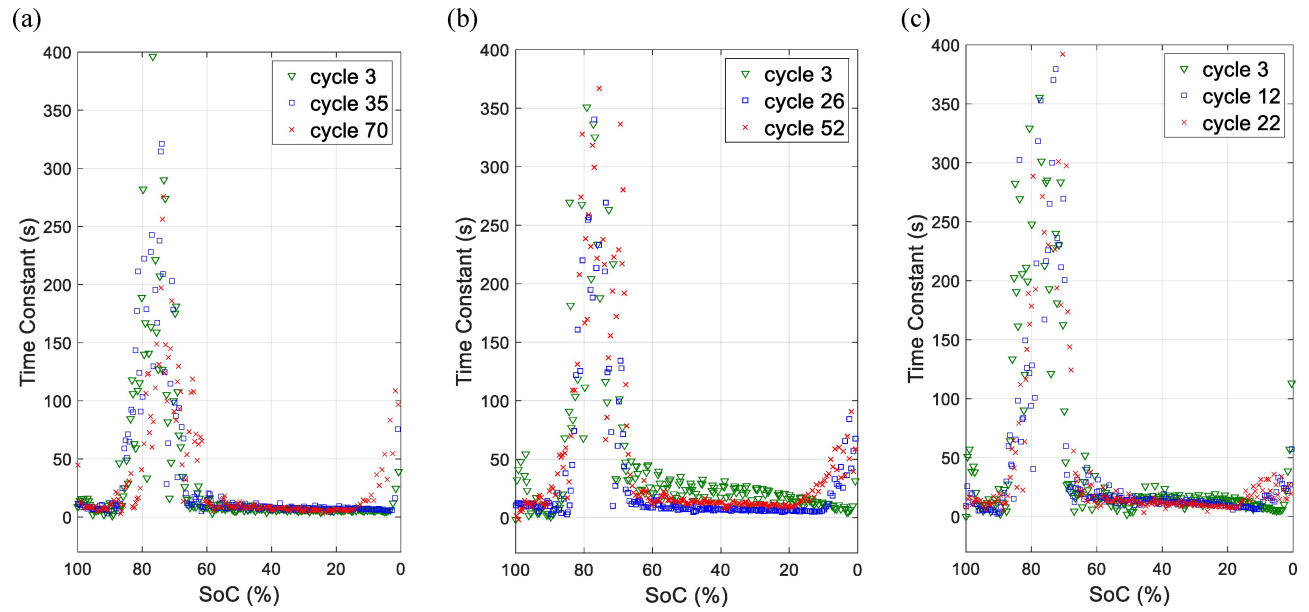

Figure 9. Li–S cell time constant ($R_p \times C_p$) at different age levels: a) 10 °C, b) 20 °C, and c) 30 °C.

cells using different electrolytes. In the present study, we tested a high-capacity pouch cell instead, and we observed 20% capacity loss after 50 cycles at 20 °C. On the other hand, looking at the power fading results shown in Figure 5(c), only 10% change in ohmic resistance is observed after 50 cycles in this study. However, an increase of 100% in the resistance is reported after 100 cycles.[56]

It should be noted that, in all the above-mentioned literature, coin cells have been studied. A more similar type of cell (i.e., pouch cell) is investigated.[57] In terms of cell specifications, the previous one[57] is a 3.4 Ah cell whereas the one used in this study has a higher capacity of 19 Ah. Looking at the model parameterization results, a range of 0.01–0.1 ohm is reported[57] for the ohmic resistance whereas our results show a change between 0.01 and 0.03 ohm. There are more studies in the literature where higher values of resistance had been reported for coin cells however, comparison between those numbers does not make sense because of the big differences in the two types of cells as discussed.[58–60] For example,[58] a comprehensive comparison between Li–S coin and pouch cells is discussed by listing all their parameters as well as their associated challenges. In addition, extensive electrochemical explorations are presented[65–67] which show miniature pouch cells degrade faster than coin cells using

© 2022 The Authors. Batteries & Supercaps published by Wiley-VCH GmbH

Research Article
doi.org/10.1002/batt.202200035
Chemistry Europe
European Chemical Societies Publishing

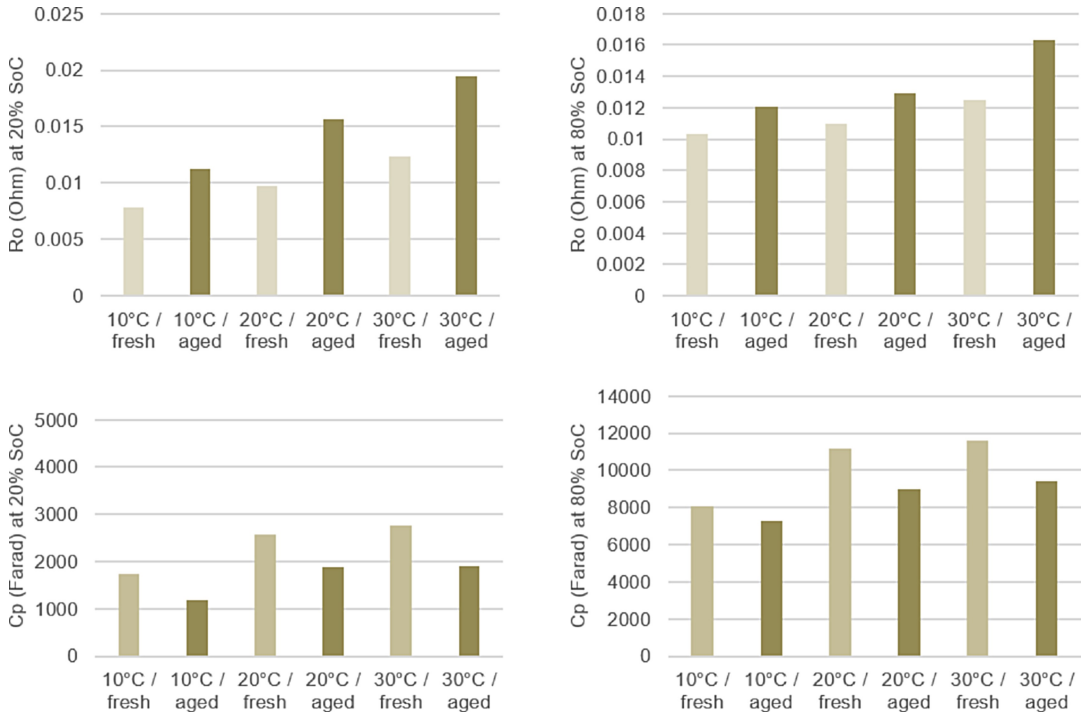

Figure 10. Li–S cell Thevenin model's parameters at three temperatures, two SoC levels, and two different ages

identical conditions, but the structural information is not comprehensive. Examining the SoH is crucial because using larger cells (for example in EV battery packs), there is less tolerance for volume changes in the stack geometry. This highlights the pressing need to use X-ray techniques to diagnose the SoH of a large Li–S pouch cell. In this paper, the OXIS prototype cells demonstrated a longer cycle life at 10 and 20 °C than those miniature, 'lab scale' pouch cells. In the following "Physical changes of Li–S cell due to ageing at various temperatures" Section, our cell metrology analysis will show how the temperature influences the gas formation inside the cell. Nevertheless, to achieve a Li–S pouch cell with a high energy density and a long cycle-life, significant efforts will be needed to address scale-up from laboratory to commercially relevant sizes. This involves material development (cathode and electrolyte), advanced characterization and improved battery management systems (BMS).

So far, the electrical performance features of the prototype Li–S pouch cell have been investigated under different age and temperature levels. In the next Section, some of the physical features of the Li–S cell are measured and analyzed.

Physical changes of Li-S cell due to ageing at various temperatures

As a complementary analysis, physical changes of the Li–S cells due to ageing are investigated in this Section. The main goal is to analyze the effect of temperature on Li–S cell's behavior and its consequences on the physical features of the cell. First, a simple visual inspection is presented in the following Section, which shows the external state of the Li–S cell. Secondly, different X-ray analyses are performed to observe the internal changes inside the Li–S cells subjected to ageing at different temperatures.

Visual inspection of Li-S cell swelling due to ageing at different temperatures

Figure 11 shows some photos of the cycled Li–S pouch cells at different temperatures. Figure 11(a and b) illustrates the top and side views of three Li–S cells which are cycled at 10 °C, 20 °C and 30 °C, respectively. According to that result, the physical deformation of the cell at 20 °C is remarkably larger than 10 °C. Indeed, the cycled cell at 10 °C is still flat without any sign of swelling. It is observed that the amount of swelling at 30 °C is even more than 20 °C. Based on the results shown in Figure 11, temperature has a direct significant impact on the swelling phenomenon in Li–S pouch cells.

Cell swelling is mainly caused by the gas formation inside the pouch cell. This phenomenon is investigated[68] using gas chromatography technique. According to that study, the main constituents at the beginning of the cycle life (after four cycles) were found to be hydrogen and nitrogen in a ratio of 3 : 1. After larger cycle numbers (around forty cycles), significant amounts of methane and ethane stemming from reductive electrolyte decomposition could be detected as well. In the next Section, X-ray tomographic imaging is performed on the 19 Ah Li–S pouch cells before and after cycling at various temperatures.

© 2022 The Authors. Batteries & Supercaps published by Wiley-VCH GmbH

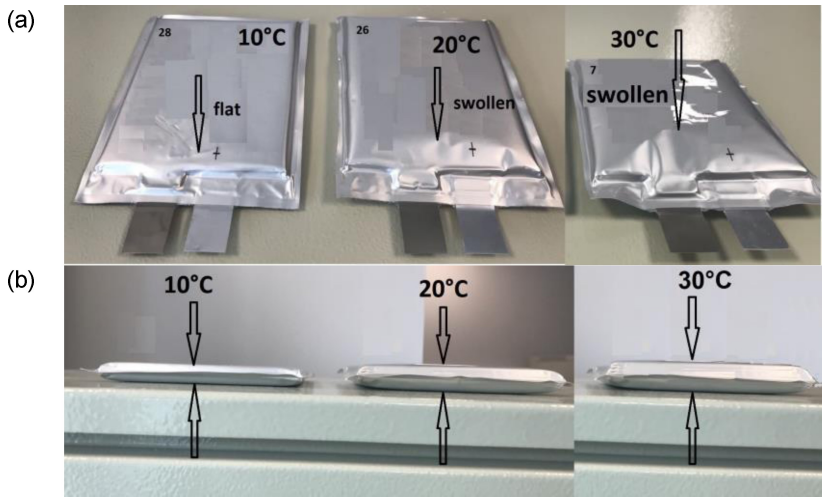

Figure 11. Li–S cells' physical status after cycling at various temperatures: a) top view, b) side view.

X-ray analysis of Li-S cell at different age and temperature levels

For the first time, the interior morphologies of large footprint Li–S pouch cells are revealed by X-ray tomographic imaging. In Figure 12, 2D and 3D macro-structure of the Li–S pouch cells under various ageing temperatures are presented. A large-format Li–S pouch cell is composed of multiple layers of electrodes, separators and current collectors stacked together. The 2D cross-sections on the y-z plane (front view) are selected between two current collectors as shown in Figure 12(a–c), whilst 2D slices on the *x-z* plane (side view) are demonstrated in Figure 12(d and f). The white, gray, and black phases are corresponding to the Cu current collector, sulfur-based cathodes, and cycled-induced gas according to X-ray attenuations. In Figure 12(e), the anode phase (Li metal) is not shown mainly because 1) the density of Li is too low (low-Z material). Therefore, when we had to use high energy to scan the large cell, X-ray will direct penetrate the Li layer, which means it hardly provides contrast, 2) due to the limited spatial resolution (ca. 20 μm), the very thinner Li layer (usually ~100 μm) might not be resolved too.

The fresh Li–S pouch cells are stored in the fridge at ca. 2~3 °C to prevent self-degradation, the X-ray CT results prove this assumption since the gaseous product is hardly found in Figure 12(a, d, g). Both uniform spacing and multiple parallel assemblies (electrodes and current collectors) are observed in fresh cell (Figure 12d). Some gas bubbles with small size can be found in Figure 12(e) when the cell was fully aged at 10 °C. The harmful gas is usually generated during cell cycling *via* electrolyte decomposition. A large amount of gas with large size was clearly observed within the Li–S cell after it was fully aged at 20 °C, as shown in Figure 12(c and f). Indeed, the Li–S cell aged at 20 °C demonstrated swelling of the cell assemblies, along with non-uniform electrode spacing (Figure 12f), indicating major degradation of the internal architecture. Moreover, the electrode defects due to its expansion after cycling, such as cracks with a size up to 300 μm, can be observed in Figure 12(c and f). This will affect the cell conductivity and lead to shortening the failure. The generated gas and electrode swelling deforms their assemblies for both 10 and 20-degree cases, but the deformation is more prominent in higher temperature case. This is also supported by accounting for the current collector (CC) numbers within the same ROI (Table 4). There are 13 CCs in 20 °C, while 21 CCs in 10 °C. Nevertheless, macro-CT experiments verify that the mechanism of volumetric expansion for Li–S cells is more complicated than Li-ion cells. While Li–S morphological swelling is attributed to the electrode expansion, gaseous products and loss of lithium inventory,[70] in Li-ion cells, the gas is considered to be the dominating factor.[71] 3D macro-structure of Li–S cells are rendered and presented in the 3rd row of Figure 12. The gaseous structure and thickness distributions were correspondingly superimposed on their 3D volume renderings. 3D gas structure and thickness distributions in Li–S cells are rendered and presented in Figure 12(h and i). The darker colors (black and purple) represent the low thickness regions, whilst the brighter colors (orange and yellow) indicate the high thickness regions. According to the degradation level, the fresh, 10 °C, and 20 °C cases can be classified as low, medium and high degradations, respectively.

In Figure 13, the application of macro-CT to inspect and quantify the SoH by tracking the gas phase is demonstrated.

Table 4. The quantification of cycle-induced gas in Li–S pouch cells.

Sample status	Surface area [mm^2]	Volume [mm^3]	Thickness [μm]				Current collector number
			min	max	Mean	SD	
@ 10 °C	822	13	80	240	119	24.9	20
@ 20 °C	2003	62	80	360	174	45.7	13

© 2022 The Authors. Batteries & Supercaps published by Wiley-VCH GmbH

Research Article
doi.org/10.1002/batt.202200035
Chemistry Europe
European Chemical Societies Publishing

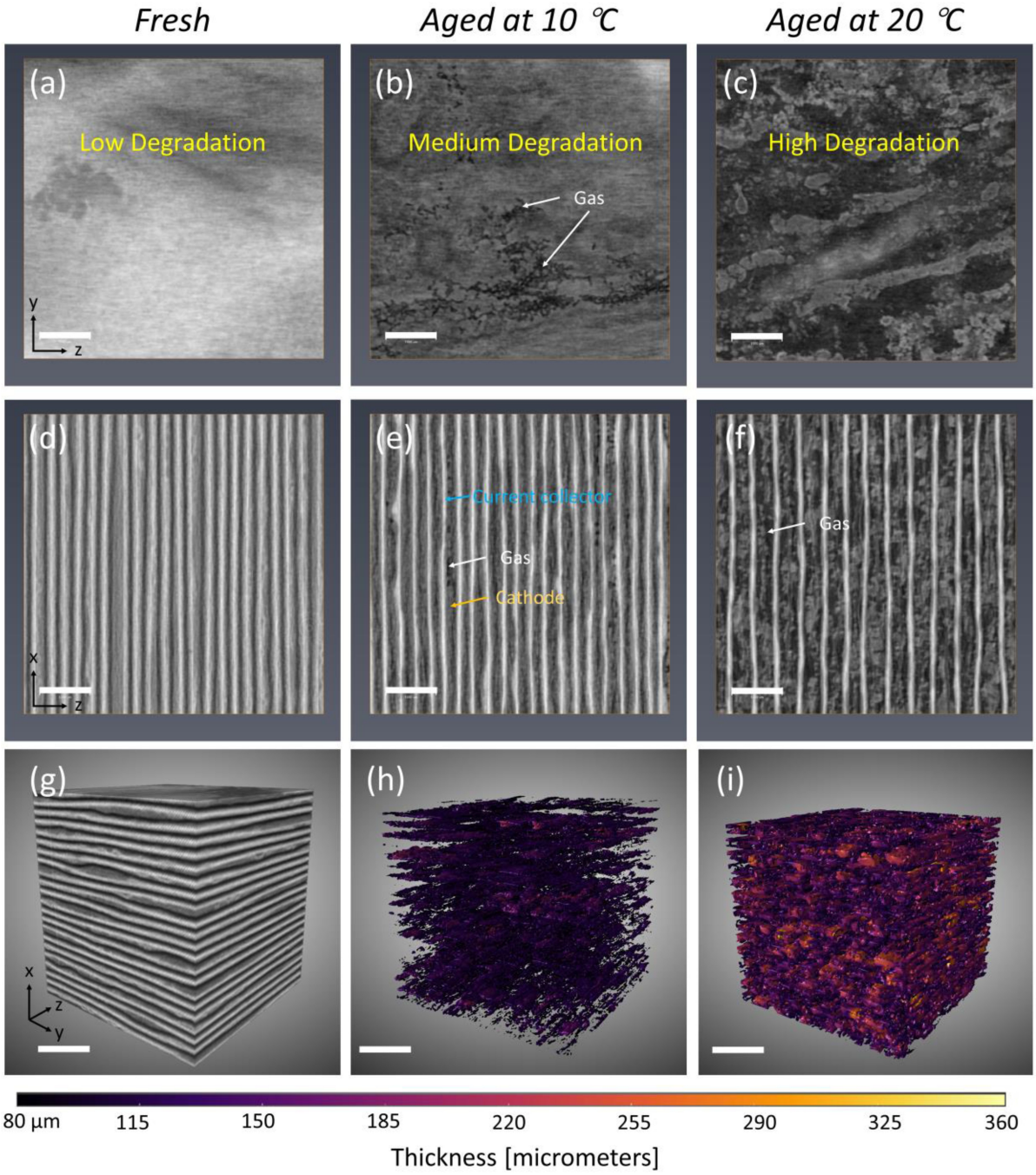

Figure 12. X-ray macro-CT of 19 Ah Li–S pouch cells when the cell is fresh (a, d, g), aged at 10 °C (b, e, h), and aged at 20 °C (c, f, i), showing the interior macro-structure under various temperatures. Three cubic sub-volumes (300×300×300 voxels), included the front (a–c) and the side view (d–f) of 2D slices, are subsequently extracted from three 19 Ah cells at the same location. The fresh sample is rendered in (g), whilst the cycle-induced gas structures are segmented, and volume rendered in 3D (h–i). Scale bars are 1 mm for all figures (a–i). The color bar at the bottom represents the thickness distribution of gas, ranging from 80 to 360 µm.

Here, the high degradation case (i.e., 20 °C) is selected to present in Figure 13(a–d). Figure 13(a) shows the 2D gas thickness profile is overlaid with the original 2D slice (Figure 12f). The color lines highlight the gas phase and indicate the associated thickness value within the FOV. 2D mappings could be stacked and rendered in 3D (Figure 13b). In total, there are 14 gaseous layers in high degradation case. Clearly, according to the thickness mappings in Figure 13(a and b), the heterogeneous gas distribution can be identified. This heterogeneity also can be decoupled by selectively visualizing the low thickness (80–220 µm) and high thickness (220–360 µm) regions respectively as shown in Figure 13(c and d). It should be noted that adjustment above thickness domains to perform the comparison is feasible. There are many thicker gas layers (assigned to yellow) within the ROI, demonstrating the cell has a considerable degradation when aged at 20 °C. In Figure 13(f),

© 2022 The Authors. Batteries & Supercaps published by Wiley-VCH GmbH

Research Article
doi.org/10.1002/batt.202200035
Chemistry Europe
European Chemical Societies Publishing

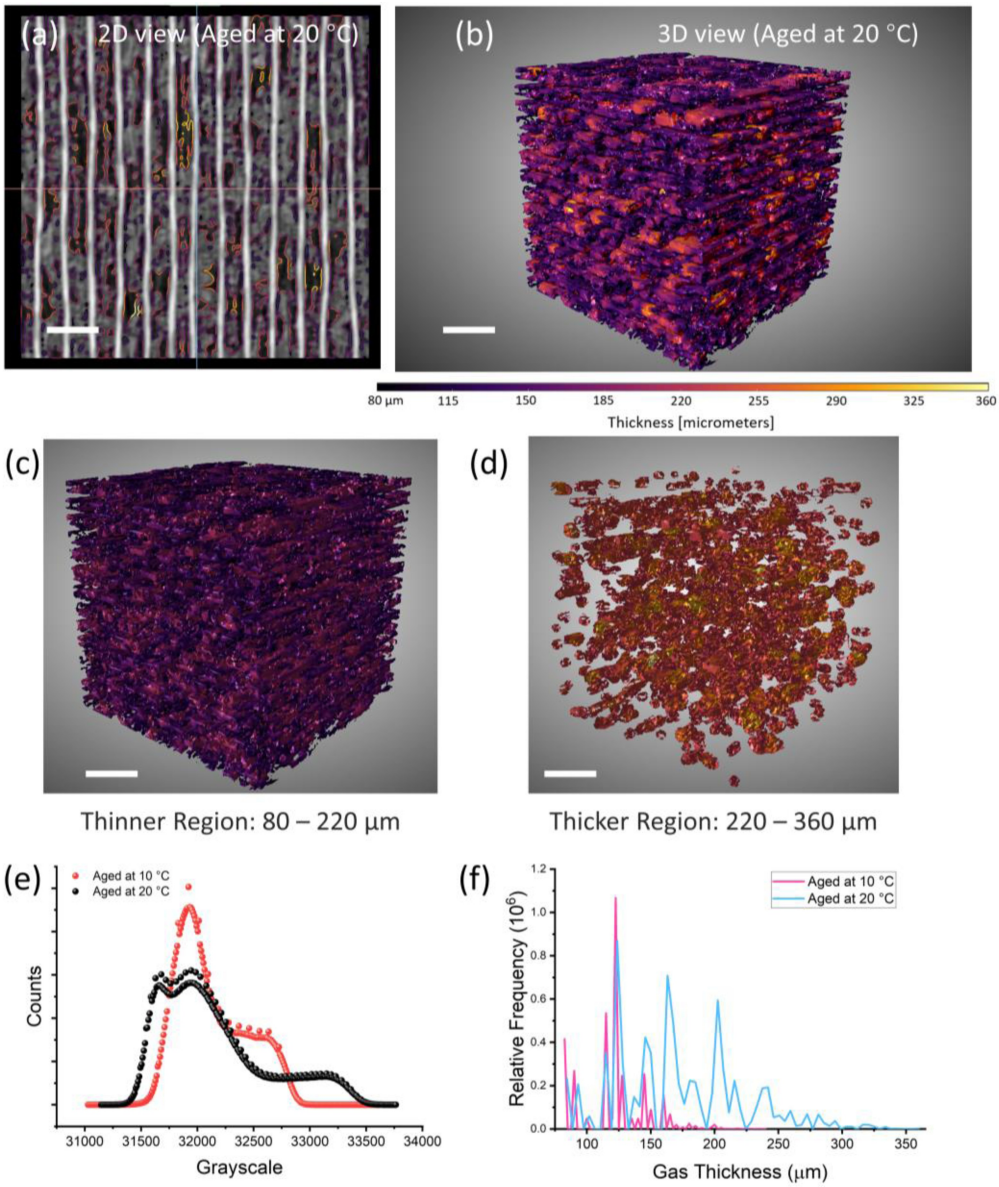

Figure 13. X-ray macro-CT quantification of the 19 Ah Li–S pouch cells. a) 2D thickness distribution of gas phase aged at 20 °C, showing its heterogeneous characteristic (overlaid with the raw image). Stacked 2D mappings are rendered in 3D displayed in b). The gaseous heterogeneity can be decoupled by selectively visualizing c) the thinner region (80–220 µm) and d) the thicker region (220–360 µm). Both (c) and (d) are extracted from (b). Scale bars are 1 mm for figures (a–d). The color bar represents the same thickness for figures (b–d), ranging from 80 to 360 µm. e) The grayscale histograms of Li–S pouch cells fully aged at 10 and 20 °C. f) The comparison of the gas thickness within Li–S pouches aged at two various temperatures.

the histograms suggest that a large amount of gas could be generated under 20 °C case because the 1st peak is observed at the lower grayscale region (ca. 31500). Also, the X-ray signal intensities is higher (from ca. 32000 to ca. 32750) when the lower temperature is used. This indicates that a temperature set at 10 °C prevents the depletion of the carbon-sulfur (C–S) cathode and thus minimize the volume expansion. Such histogram range of S–C cathode was investigated.[72]

The distributions of gas thickness are plotted in Figure 13(f) to compare the effect of temperature on Li–S cell degradation. It is obvious to observe the 20-degree case (green bars, high degradation) have wider and larger thickness range than 10-degree case (purple bars, medium degradation). The peak value shifts from the left to the right, proving the prior 3D observation and the thickness value is increased under the higher temperature. Indeed, in Table 4, the average gas thickness increases from 119 to 174 µm when the temperature increases from 10 to 20 °C. The higher temperature significantly facilitates the gas generation as its volume increases from 13 to 62 mm^3, indicating the huge volume expansion. Furthermore, the surface area increases from 822 to 2003 mm^2, suggesting the gas bubbles (Figure 12h) could be replaced by the gas layers with the uniformed thickness (Figure 12i) when cell ageing under the higher temperature (i.e., 20 °C). Such temperature-dependent behavior has been studied microscale, it is believed that the low temperature may increase Coulombic

© 2022 The Authors. Batteries & Supercaps published by Wiley-VCH GmbH

efficiency and prolong cycle life through lower chemical reactivity (especial Li metal) in the absence of short-circuits, whlist higher temperatures lead to unstable SEI formation, poor Coulombic efficiency, and electrolyte degradation.[73] We suspect that temperature has a strong link with the viscosity of electrolytes that affects the cycle performance as shown in "Capacity fade and power fade of Li–S cell due to ageing at various temperatures" and "Performance change of Li–S cell due to ageing at various temperatures" Sections. It is widely recognized that a higher temperature will have a lower viscosity value. Therefore, at lower temperatures (10 °C), the higher viscosity electrolyte will impede electrolyte transport during formation and ageing. The formation of the SEI may therefore be more uniform than other higher temperature cases (20 and 30 °C). Moreover, the sluggish movement of electrolytes due to the higher viscosity could minimize the shuttle effect, and thus fewer polysulfides (Li_2S_x, $4 < x < 8$) will be transported. A higher temperature could facilitate electrolyte movement, the heterogenous SEI could be formed, and a large amount of gas products will be also generated due to the faster electrolyte depletion. As a result, the resistance (R_0) is expected to be increased at high temperature which leads to a shorter cyclic life. The increase of R_0 could be attributed to the formation of a thicker SEI layer and associated structural degradation with progressive cycling under higher temperature.[74] It is suggested that the gas generation and delamination between electrodes and current collector affect the cell polarization. Our macro-CT results show that at higher temperature more gas would be created. As a consequence, the electrode layer delamination is observed which leads to the C_p decrease.

Conclusion

In this study, a combination of two advanced methods, ECN modelling using FFRLS and X-ray tomography, was used to investigate the cycle life performance of a Li–S pouch cell and the effect of temperature on it. State-of-the-art 19 Ah prototype Li–S cells were subjected to a real-world duty cycle until they degraded. After running the ageing tests, three types of analysis were conducted as follows:

1. Firstly, the capacity fade and the power fade of Li–S cells were investigated at three temperatures: 10 °C, 20 °C and 30 °C. Two main outcomes were obtained from that analysis: (i) it was observed that the power fade happens with a slower rate (almost half) than the capacity fade in Li–S cells. (ii) it was observed that the temperature has a significant effect on both the capacity and power fades. The best performance (i.e., the slowest degradation rate) was achieved at 10 °C whereas the worst case happened at 30 °C.
2. Secondly, the effects of ageing on Li–S cell's performance are investigated using an ECN model by considering the effect of temperature. The Thevenin ECN model was parameterized under different age and temperature conditions using FFRLS technique. Each individual parameter of the model was analyzed separately to investigate its changes in response to cycling. In addition, the effect of temperature on each of those parameters was investigated. Two outcomes of those analyses are: i) parameters U_{oc} and R_p have been affected less than parameters R_0 and C_p as the result of cycling. ii) the most and the least changes in the ECN parameters R_0 and C_p, were observed at 30 °C and 10 °C respectively.
3. Thirdly, physical changes of Li–S cells due to cycling were analyzed with a focus on the effect of temperature. All Li–S cells were analyzed under identical conditions, X-ray tomography result confirms the ECN models, providing strong evidence that temperature has a direct and significant impact on the swelling phenomenon in Li–S pouch cells where the most and the least swelling were measured at 30 °C and 10 °C respectively. In addition, for the first time, the volumetric expansion and interior morphologies of commercial Li–S prototype cells under different ageing temperatures were investigated. X-ray macro-CT was used to monitor the cell SoH and quantify the gas thickness. It was found that the lower temperature at 10 °C can mitigate cell degradation and prolong its life cycle which matches the analytical models. The thickness change was mostly due to cracked electrodes and gas formation.

In this study, we demonstrated a case study using macro-CT as a diagnostic tool to examine the battery SoH. The Li–S pouch cells showed a considerable swelling during ageing particularly at 20 and 30 °C. The Li–S structure expansion may be more severe than that in the Li-ion pouch cell, which present engineering challenges for the next generation Li–S cells. For instance, the development of a functional separator to enhance thermal stability may provide promising solutions.[67] Direct 3D visualization at mid-to-large length scales complements the previous microscale studies, identifying cell-level changes (geometric deformation, electrode alignment and electrolyte depletion) and electrode-scale phenomena (i.e., electrode/gas thickness and macro-cracking). Nevertheless, more systematic in-situ CT studies as a function of SoC and SoH are needed to fully understand the temperature-dependent degradation in large footprint Li–S cells. The multiscale and correlative X-ray tomography, in particular the hierarchical phase-contrast tomography (HIP-CT),[75] could provide an opportunity to advance the Li–S cell development.

Furthermore, in future work, development of an adaptive algorithm addressing the formation strategies during early cycle life and generating a uniform and robust solid-electrolyte interphase (SEI) layer, will be explored. This could help in mitigating the Li dendrite formation and prolong the Li–S life.

Acknowledgments

The authors thank OXIS Energy for their help and support. This work was funded by the European Commission under grant agreement 814471, Innovate UK under grant TS/R013780/1 and the Faraday Institution (EP/S003053/1; FIRG014 and FIRG027). In addition, P.R.S acknowledges funding from The Royal Academy of

© 2022 The Authors. Batteries & Supercaps published by Wiley-VCH GmbH

Engineering (CiET1718/59). The data used in this article is described in CORD at 10.17862/cranfield.rd.17163545.

Conflict of Interest

The authors declare no conflict of interest.

Data Availability Statement

The data that support the findings will be available in The Effect of Temperature on Lithium-Sulfur Battery Performance at https://cord.cranfield.ac.uk[10.17862/cranfield.rd.17163545] following an embargo from the date of publication to allow for commercialization of research findings.

Keywords: egradation modelling · electrochemistry · energy Conversion · lithium-sulfur battery · temperature · 3D gas thickness · X-ray tomography

[1] G. Benvenistea, H. Rallob, L. Canals Casalsa, A. Merinob, B. Amante, *J. Environ. Manage.* **2018**, *226*, 1–12.
[2] D. M. Briesk, A. Warneckeb, D. U. Sauera, *J. Energy Storage* **2021**, *43*, 103148.
[3] A. F. Hofmann, D. N. Fronczek, W. G. Bessler, *J. Power Sources* **2014**, *259*, 300–310.
[4] L. Lam, P. Bauer, *IEEE Trans. Power Electron* **2013**, *28*, 5910–5918.
[5] J. B. Robinson, K. Xi, R. V. Kumar, A. C. Ferrari, H. Au, M-M. Titirici, A. Parra-Puerto, A. Kucernak, S. D. S. Fitch, N. Garcia-Araez, Z. L. Brown, M. Pasta, L. Furness, A. J. Kibler, D. A. Walsh, L. R. Johnson, C. Holc, G. N. Newton, N. R. Champness, F. Markoulidis, C. Crean, R. C. T. Slade, E. I. Andritsos, Q. Cai, S. Babar, T. Zhang, C. Lekakou, N. Kulkarni, A. J. E. Rettie, R. Jervis, M. Cornish, M. Marinescu, G. Offer, Z. Li, L. Bird, C. P. Grey, M. Chhowalla, D. D. Lecce, R. E. Owen, T. S. Miller, D. J. L. Brett, S. Liatard, D. Ainsworth, P. R. Shearing, *J. Phys. Energy* **2021**, *3*, 031501.
[6] S. Dörfler, S. Walus, J. Locke, A. Fotouhi, D. J. Auger, N. Shateri, T. Abendroth, P. Härtel, H. Althues, S. Kaskel, *Energy Technol.* **2021**, *9*, 2000694.
[7] Y. Huang, M. Shaibani, T. D. Gamot, M. Wang, P. Jovanović, M. C. Dilusha Cooray, M. Sharifzadeh Mirshekarloo, R. J. Mulder, N. V. Medhekar, M. R. Hill, M. Majumder, *Nat. Commun.* **2021**, *12*: 5375.
[8] A. Fotouhi, D. J. Auger, L. O'Neill, T. Cleaver, S. Walus, *Energies* **2017**, *10*, 1937.
[9] K. Propp, M. Marinescub, D. J. Auger, L. O'Neill, A. Fotouhi, K. Somasundaramc, G. J. Offer, G. Mintonc, S. Longo, M. Wild, V. Knap, *J. Power Sources* **2016**, *328*, 289–299.
[10] C. Xu, T. Cleary, D. Wang, G. Li, C. Rahn, D. Wang, R. Rajamani, H. K. Fathy, *J. Power Sources* **2021**, *489*, 229–495.
[11] Z. Huang, D. Zhang, L. D. Couto, Q.-H. Yang, S. J. Moura, *arXiv:2101.10436*, **2021**.
[12] A. Fotouhi, D. J. Auger, K. Propp, S. Longo, *Eighth Int. Conf. PEMD, IET Power Electron.* **2017**, *10*.
[13] A. Fotouhi, D. J. Auger, K. Propp, S. Longo, *IEEE Trans. Power Electron.* **2018**, *33*, 5847–5859.
[14] N. Shateri, Z. Shi, D. J. Auger, A. Fotouhi, *IEEE Trans. Veh. Technol.* **2021**,70, 212–224.
[15] K. Propp, D. J. Auger, A. Fotouhi, S. Longo, V. Knap, *J. Power Sources* **2017**, *343*, 254–267.
[16] N. A. Canasa, K. Hirosea, B. Pascuccia, N. Wagnera, K. A. Friedricha, R. Hiesgen, *Electrochim. Acta* **2013**, *97*, 42–51.
[17] H.-J. Peng, T. Z. Hou, Q. Zhang, J. Q. Huang, X. B. Cheng, M. Q. Guo, Z. Yuan, L. Y. He, F. Wei, *Adv. Mater. Interfaces* **2014**, *7*, 140022.
[18] E. Peled, M. Goor, I. Schektman, T. Mukra, Y. Shoval, D. Golodnitsky, *J. Electrochem. Soc.* **2017**, *164* A5001-A5007.
[19] Q. Lemarié, H. Idrissi, E. Maire, P. X. Thivel, F. Alloin, L. Roué, *J. Power Sources* **2020**, *477*, 228374.
[20] X. Feng, M. K. Song, W. C. Stolte, D. Gardenghi, D. Zhang, X. Sun, J. Zhu, E. J. Cairns, J. Guo, *Phys. Chem. Chem. Phys.* **2014**, *16*, 16931–16940.
[21] L. Zielke, C. Barchasz, S. Waluś, F. Alloin, J.-C. Leprêtre, A. Spettl, V. Schmidt, A. Hilger, I. Manke, J. Banhart, R. Zengerle, S. Thiele, *Sci. Rep.* **2015**, *5*, 10921.
[22] A. Robba, C. Barchasz, K. Bucar, M. Petric, M. Žitnik, K. Kvashnina, G. B. M. Vaughan, R. Bouchet, F. Alloin, M. Kavčič, *J. Phys. Chem. Lett.* **2020**, *11*, 5446–5450.
[23] C. Tan, T. M. M. Heenan, R. F. Ziesche, S. R. Daemi, J. Hack, M. Maier, S. Marathe, C. Rau, D. J. L. Brett, P. R. Shearing, *ACS Appl. Mater. Interfaces* **2018**, *1*, *9*, 5090–5100.
[24] V. Vanpeene, A. Etiemble, A. Bonnin, E. Maire, L. Roué, *J. Power Sources* **2017**, *350*, 18–27.
[25] G. Tonin, G. B. M. Vaughan, R. Bouchet, F. Alloin, M. D. Michiel, C. Barchasz, *J. Power Sources* **2020**, *468*, 228287.
[26] N. Shateri, D. J. Auger, A. Fotouhi, J. Brighton, *IEEE Trans. Transp. Electrification* **2021**, *7*, 1324–1338.
[27] S. Gohari, V. Knap, M. R. Yaftian, *Sustainability* **2021**, *13*, 9473.
[28] V. Knap, D. J. Auger, K. Propp, A. Fotouhi, D. Stroe, *Energies* **2018**, *11*, 2133.
[29] M. Ecker, J. B. Gerschler, J. Vogel, S. Käbitz, F. Hust, P. Dechent, D. Sauer, *J. Power Sources* **2012**, *215*, 248–257.
[30] T. Waldmann, M. Wilka, M. Kasper, M. Fleischhammer, M. Wohlfahrt-Mehrens, *J. Power Sources* **2014**, *262*, 129–135.
[31] S. F. Schuster, T. Bach, E. Fleder, J. Müller, M. Brand, G. Sextl, A. Jossen, *J. Energy Storage* **2015**, *1*, 44.
[32] M. Bauer, C. Guenther, M. Kasper, M. Petzl, M. A. Danzer, *J. Power Sources* **2015**, *283*, 494.
[33] L. Bodenes, R. Naturel, H. Martinez, R. Dedryvère, *J. Power Sources* **2013**, *236*, 265–275.
[34] J. Vette, P. Nováka, M. R. Wagnerb, C. Veitb, K. Möller, J. O. Besenhardb, M. Winter, M. Wohlfahrt-Mehrens, C. Vogler, A. Hammouche, *J. Power Sources* **2005**, *147*, 269–281.
[35] G. Ning, B. Haran, B. N. Popov, *J. Power Sources* **2003**, *117*, 160–169.
[36] J. Becker, M. Lelie, M. Jansen, D. U. Sauer, *Conference: 11. Symposium: Hybrid- und Elektrofahrzeuge*, **2014**.
[37] M. Ouyanga, Z. Chua, L. Lua, J. Lia, X. Hana, X. Fenga, G. Liu, *J. Power Sources* **2015**, 286 309–320.
[38] M. Fleischhammer, T. Waldmann, G. Bisle, B.-I. Hogg, M. Wohlfahrt-Mehrens, *J. Power Sources* **2015**, *274*, 432–439.
[39] J. Jaguemont, L. Boulon, P. Venet, Y. Dubé, A. Sari, *IEEE twenty forth Int. Symp. Ind. Electron.* **2015**, 1550–4991.
[40] D. Ouyang, Y. He, J. Weng, J. Liu, M. Chen, J. Wang, *RSC Adv.* **2019**, *9*, 9053–9066.
[41] Z. Lei, Y. Zhang, X. Lei, *Int. J. Heat Mass Transfer* **2018**, *121*, 275–281.
[42] L. Ghadbeigi, B. Day, K. Lundgren, T. D. Sparks, *Energy Rep.* **2018**, *4*, 303–307.
[43] http://www.oxisenergy.com.
[44] T. J. Barlow, S. Latham, I. S. McCrae, P. G. Boulter, *A reference Book of driving cycles for use in the measurement of road vehicle emissions*, Wokingham: TRL Ltd, **2009**.
[45] Low Carbon Vehicle Partnership, Testing & Accreditation – LCEB Certification, [Online]. Available: https://www.lowcvp.org.uk/initiatives/lceb/lceb-testing.htm, **2018**.
[46] V. C. Serra, A. Fotouhi, M. Soleymani, D. J. Auger, *Int. J. Powertrains* **2020**, *9*, 265–288.
[47] A. Fotouhi, D. J. Auger, K. Propp, S. Longo, M. Wild, *Renewable Sustainable Energy Rev.* **2016**, *56*, 1008–1021.
[48] H. He, R. Xiong, J. Fan, *Energies* **2011**, *4*, 582–598.
[49] A. Fotouhi, D. J. Auger, K. Propp, S. Longo, R. Purkayastha, L. O'Neill, S. Walus, *IEEE Trans. Veh. Technol.* **2017**, *66*, 7711–7721.
[50] Z. M. Salameh, M. A. Casacca, W. A. Lynch, *IEEE Trans. Energy Convers.* **1992**, *7*, 93–98.
[51] C. Paleologu, J. Benesty, S. Ciochina, *IEEE Signal Process. Lett.* **2008**, *15*, 597–600.
[52] W. K. Yung, K. F. Man, *IFAC Proceedings Volumes* **1993**, *26*, 331–334.
[53] S. Risse, N. A. Canas, N. Wagner, E. Hark, M. Ballauff, K. A. Friedrich, *J. of Power Sources* **2016**, *323*, 107–114.
[54] N. A. Canas, K. Hirose, B. Pascucci, N. Wagner, K. A. Friedrich, R. Hiesgen, *Electrochim. Acta* **2013**, *97*, 42–51.
[55] J. Yan, X. Liu, B. Li, *Adv. Sci.* **2016**, *3*, 1600101.
[56] M. Safa, Y. Hao, A. Chamaani, E. Adelowo, N. Chawla, C. Wang, B. El-Zahab, *Electrochim. Acta* **2017**, *258*, 1284–1292.
[57] D. I. Stroe, V. Knap, M. Swierczynski, E. Schaltz, *IEEE Trans. Ind. Appl.* **2019**, *55*.

© 2022 The Authors. Batteries & Supercaps published by Wiley-VCH GmbH

[58] S. Dorfler, H. Althues, P. Hartel, T. Abendroth, B. Schumm, S. Kaskel, *Joule* **2020**, *4*, 539–554.
[59] W. Zhang, S. Li, A. Zhou, H. Song, Z. Cui, L. Du, *Molecules* **2021**, *26*, 6341.
[60] X.-B. Cheng, C. Yan, J.-Q. Huang, P. Li, L. Zhu, L. Zhao, Y. Zhang, W. Zhu, S.-T. Yang, Q. Zhang, *Energy Storage Mater.* **2017**, *6*, 18–25.
[61] A. Fotouhi, K. Propp, D. J. Auger, S. Longo, *Behaviour of Lithium-Ion Batteries in Electric Vehicles*, **2018**.
[62] A. Hoke, A. Brissette, D. Maksimović, A. Pratt, K. Smith, *IEEE Veh. Power Propuls. Conf.* **2011**.
[63] P. Malysz, J. Ye, R. Gu, H. Yang, A. Emadi, *IEEE Trans. Veh. Technol.* **2016**, *65*, 4512–4522.
[64] A. Guha, A. Patra, *IEEE Trans. Transp. Electrification.* **2018**, *4*, 135–146.
[65] M. Weinberger, M. Wohlfahrt-Mehrens, *Electrochim. Acta* **2016**, *191*, 124–132.
[66] H–S. Kang, E. Park, J. Y. Hwang, H. Kim, D. Aurbach, A. Rosenman, Y. K. Sun, *Adv. Mater.* **2016**, *6(6)*, 1600052.
[67] R. Song, R. Fang, L. Wen, Y. Shi, S. Wang, F. Li, *J. of Power Sources.* **2016**, *301*, 179–186.
[68] H. Schneider, T. Wei, C. Scordilis-Kelley, J. Maeyer, K. Leitner, H. Peng, R. Schmidt, J. Tomford, *Electrochim. Acta* **2017**, *243*, 26–32.
[69] W. Du, R. E. Owen, A. Jnawali, T. P. Neville, F. Iacoviello, Z. Zhang, S. Liatard, D. J. L. Brett, P. R. Shearing, *J. of Power Sources.* **2022**, *520*, 1, 230818.
[70] S. Waluś, G. Offer, I. Hunt, Y. Patel, T. Stockley, J. Williams, R. Purkayastha, *Energy Storage Mater.* **2018**,10, 233–45.
[71] W. Du, R. E. Owen, A. Jnawali, T. P. Neville, F. Iacoviello, Z. Zhang, S. Liatard, D. J. Brett, P. R. Shearing, *J. Power Sources.* **2022**, *520*, 230818.
[72] W. Du, Z. Hao, F. Iacoviello, L. Sheng, S. Guan, Z. Zhang, D. J. Brett, F. R. Wang, P. R. Shearing, *Small Methods.* **2021**, 5, 2001193.
[73] K. R. Adair, M. N. Banis, Y. Zhao, T. Bond, R. Li, X. Sun, *Adv. Mater.* **2020**, *32*, 2002550.
[74] J. P. Pender, G. Jha, D. H. Youn, J. M. Ziegler, I. Andoni, E. J. Choi, A. Heller, B. S. Dunn, P. S. Weiss, R. M. Penner, C. B. Mullins, *ACS Nano.* **2020**, *14*, 2, 1243–1295.
[75] C. L. Walsh, P. Tafforeau, W. L. Wagner, D. J. Jafree, A. Bellier, C. Werlein, M. P. Kühnel, E. Boller, S. Walker-Samuel, J. L. Robertus, D. A. Long, J. Jacob, S. Marussi, E. Brown, N. Holroyd, D. D. Jonigk, M. Ackermann, P. D. Lee, *Nat. Methods.* **2021**, *18*, 1532–1541.

Manuscript received: January 19, 2022
Revised manuscript received: February 22, 2022
Version of record online: April 1, 2022

© 2022 The Authors. Batteries & Supercaps published by Wiley-VCH GmbH

https://dspace.org/

Investigation of the effect of temperature on lithium-sulfur cell cycle life performance using system identification and x-ray tomography

Shateri, Neda; Auger, Daniel J.; Fotouhi, Abbas; Brighton, James; Du, Wenjia ...

2022-04-01
Wiley
https://doi.org/10.1002/batt.202200035
Shateri N, Auger D, Fotouhi A, et al., (2022) Investigation of the effect of temperature on lithium-sulfur cell cycle life performance using system identification and x-ray tomography, Batteries and Supercaps, Volume 5, Issue 8, August 2022, Article number e202200035

Downloaded from a DSpace repository. https://dspace.org/